Characterization of optical fiber imaging bundles for swept-source optical coherence tomography

Helen D. Ford* and Ralph P. Tatam

Department of Engineering Photonics, School of Engineering, Cranfield University, Cranfield, Bedford, MK43 0AL, UK

*Corresponding author: h.d.ford@cranfield.ac.uk

Received 19 October 2010; revised 17 December 2010; accepted 17 December 2010;
posted 21 December 2010 (Doc. ID 136812); published 3 February 2011

Fiber imaging bundles have been investigated for use in endoscopic optical coherence tomography (OCT) systems, to obviate the requirement for scanning components within the endoscope probe section. Images have been acquired using several optical configurations, two of which are common path in design. Configurations have been selected as having potential for miniaturization and inclusion in endoscopic-type systems, since the advantages of employing imaging bundles are most clearly seen in this type of system. The various types of bundle available are described, and the properties of the leached bundles used here are discussed in detail, with reference to their effect upon the performance of OCT systems. Images are displayed from measurements made on a range of samples. © 2011 Optical Society of America

OCIS codes: 110.4500, 110.2350, 060.2370.

1. Introduction

Optical coherence tomography (OCT) is an adaptation of low-coherence interferometry (LCI). LCI was developed for noncontact surface profiling [1–3], whereas OCT refers to the same technique applied to subsurface imaging of semitransparent materials. The LCI technique comprises an interferometer, used with a broadband light source, in which one of the reflectors is replaced by the sample of interest and the other, known as the reference reflector, scans rapidly and linearly over a short distance parallel to the optical axis of the system, to modulate the interferometer path-length difference. Interference fringes are generated when paths within the system match to within the source coherence length, which is typically a few micrometers to a few tens of micrometers, thereby providing a relative measurement of distance to the sample surface. The depth resolution of the technique is thus set by the temporal coherence of the broadband optical source. Two-dimensional (2D) and three-dimensional information is obtained by scanning the interrogating beam across the surface of the sample. In recent years, OCT has generated enormous interest [4,5], particularly for imaging biological tissue, since subsurface structures of the sample are imaged with a very high spatial resolution. An alternative implementation of the OCT technique is now generally preferred, in which the path-length difference is fixed and a laser source, with a coherence length of a few centimeters, sweeps rapidly and linearly in wavelength over a range of about 100 nm. Swept-source systems allow fast acquisition, and the image contrast is often better than in time-domain systems [6]. The image in swept-source OCT is generated from a fast Fourier transform (FFT) of data acquired by sampling the interferometer output many times during the laser sweep [7].

OCT in turbid biological tissue, both *in vitro* and *in vivo*, is finding widespread applications in the diagnosis and treatment of medical problems, particularly disorders of the internal structures of the eye [8] and cancers of the epithelial tissues of the human body [9,10]. For internal investigations, such as measurements of the gastrointestinal tract, endoscopic systems using optical fiber components have been developed [11]. Typically, these use one of two techniques to obtain 2D images; either a right-angle prism rotates within the probe, turning the beam

0003-6935/11/050627-14$15.00/0

through 90° and sweeping it in a circle concentric with the probe axis [12], or a miniaturized scanning mirror (or microelectromechanical system device) is incorporated within the probe to allow greater choice over the scanning direction [13].

We have developed swept-source LCI/OCT systems, incorporating one or more optical fiber imaging bundles within an endoscopic probe. By coupling light into different fibers within the imaging bundle, multiple points on the sample surface are addressed without any scanning at the probe end of the system. Our interest in low-coherence systems arises from consideration of the requirements for endoscopic imaging in clinical OCT applications, but there are also numerous nonbiological situations requiring noninvasive thickness measurements or internal structural analysis, for which OCT is a good candidate. These include, for example, subsurface investigation of resin composites [14], manufacture of sheet materials [15], and art conservation projects [16]. The introduction of imaging fiber bundles to OCT systems allows a completely passive endoscopic probe section to be constructed. Our first publication proposing imaging bundles for use in OCT [17] was published almost simultaneously with another paper on the same subject [18] in 2005. The work discussed in both these papers was based on time-domain systems. We investigated an 800 nm OCT system in which all fibers of an imaging bundle were illuminated simultaneously, the signal being collected on a CCD camera [19]. While partially successful, this system was slow because the camera frame rate was only 25 Hz. Phase drift during the acquisition time was problematic, as were large variations of intensity across the image. In recent years a number of other researchers have also reported bundle-based OCT systems. A common-path Fourier-domain system has been described [20], and work has been reported on removal of the image pixelation effect resulting from the optical dead space between fiber cores in the bundle [21].

To the best of our knowledge, this paper is the first report of a bundle-based OCT system using swept-source processing. It describes a scheme in which a focused beam is scanned across the input face of the bundle to address each fiber in turn. The information from the different fibers is multiplexed in time. Although transverse scanning components are required for this technique, they are removed to the input end of the instrument, remote from the measurement region. The leached imaging bundles used in this investigation, described in detail below, have outer diameters of only 1–3 mm and are extremely flexible, making them highly appropriate for endoscopic applications. In principle, the removal of active beam-scanning components from the endoscopic head allows very small probe diameters to be achieved, especially if Gradient-index (GRIN)-rod lenses are incorporated into the probe end. The removal of scanning from the probe would be advantageous in situations where access is difficult, such as internal OCT measurements on live patients, or in engineering environments where it is preferable not to introduce electrical signals, such as measurements near inflammable or explosive gases. The miniature scanning components required for integration into an endoscopic OCT probe head are expensive and the experimental design can be awkward, resulting in larger probe dimensions than may be tolerated for some applications. Such probes are typically side viewing [11], requiring the sample surface to be positioned to the side of the probe and perpendicular to the optical axis. The use of bundles, however, would allow both side-viewing and forward-viewing configurations to be designed with only minor changes required in the probe-head optics. This paper explores the characteristics of three optical configurations for swept-source OCT using fiber imaging bundles.

2. Optical and Data Acquisition Systems

Figure 1 shows one of the configurations investigated for a swept-source OCT system incorporating a fiber imaging bundle. Light from the swept source emerges via a single-mode fiber, which is connected to a broadband optical circulator using fiber connectors, angle polished to avoid backreflections into the laser. The circulator delivers the laser output, minus losses, to the bundle input optics. A pair of lenses focuses the light to a small beam waist appropriate for coupling into a single core of the bundle, and a rotating mirror mounted on a galvanometer scanner scans the beam across the input face of the bundle. If paired galvo-scanners are used, a 2D region of the sample can be addressed. The optics used are described in greater detail below.

The figure shows a common-path system [22], in which both probe and reference beams travel identical paths through the bundle at all times. Light from the output of the bundle is focused onto a mirror, and the OCT interferometer is formed by positioning a beam splitter cube in the focused probe beam, to divert a portion of the optical power onto the surface of the sample. We used a custom broadband beam splitter with a nominal 80% reflection/20% transmission, to direct most of the light onto the sample. In

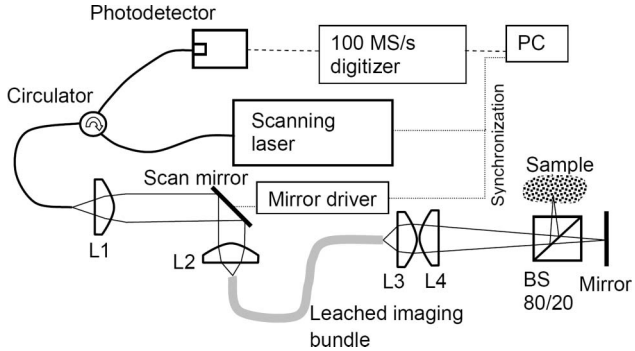

Fig. 1. Configuration 1. Swept-source, common-path OCT system incorporating an imaging fiber bundle, with miniature Michelson interferometer formed at output of bundle. BS, beam splitter; L1, L2, L4, $f = 18.5$ mm; L3, $f = 8.0$ mm.

practice, it was closer to a 70/20 split with 10% loss. Backscattered light from the sample and reference mirror returns through the bundle, where it is collected by the circulator and delivered to a photodetector. The path-length difference is set to be less than the instantaneous coherence length of the laser, such that the two returning beams combine interferometrically. The lateral resolution scales linearly with the magnification at the probe end of the sample bundle; for a magnification of 1, it is 10.6 μm, the same as the core spacing. Axial resolution, calculated from the center wavelength of 1280 nm and wavelength sweep of 90 nm, is about 8 μm.

The source used in this system is a Santec HSL-2000 scanning laser with a center wavelength of 1330 nm, a wavelength scanning rate of 20 kHz, and a wavelength sweep of about 100 nm, which is very close to linear as a function of time. The slight deviation from nonlinearity is well characterized [23] and has been corrected for in the data. The maximum instantaneous power from the laser fiber pigtail is about 13 mW, occurring close to 1350 nm. The optical signal, returning from the OCT system through the circulator, is incident on a fiber-coupled, low-noise InGaAs photodetector, with a 3 dB bandwidth of 15 MHz and an output response of 51×10^3 V/W. Data acquisition is performed by a National Instruments PXI-5122 digitizer card, mounted in an external chassis and controlled from a personal computer by NI-SCOPE LabVIEW software. The analog inputs to the digitizer are converted to a 14 bit digital signal, with a maximum sampling rate of 100 MS s^{-1}. The repeat period of the laser wavelength sweep is 50 μs, with a duty cycle of about 80%. For an imaging depth of 2 mm in air, applying the Nyquist sampling criterion, it is necessary to collect more than 450 samples within the sweep period, or 600–800 for the same depth in a high-index sample. In our system, data points are sampled at equal wavelength intervals. The Fourier transform required to extract spatial information requires data points equally spaced in optical frequency, for which resampling of the data is required. Given the 20 kHz sweep rate of the laser, we use an acquisition rate of 33 MS s^{-1}, which results in data sets of about 1350 values per sweep. Resampled sets of 800 points, equally positioned in frequency space, are then calculated.

A batch of typically 600 data sets is collected during each mirror scan, containing the information to generate one 2D image of 600 × 400 pixels. The batch start time is synchronized to the rotational position of the mirror by a signal from the mirror controller, driven by a sawtooth waveform generated either from the computer or an external source. Within this batch, acquisition of each data set is triggered by a TTL output pulse from the laser.

AC frequencies higher than half the sampling rate, i.e., 16.5 MHz, present at the analog input connector, give rise to aliased frequencies in the digitized signal, and are best discarded before the digitization process takes place. Thus the 15 dB bandwidth of the detector used here is well suited to measurement at the 33 MHz sampling rate.

3. Properties of Imaging Fiber Bundles

Coherent optical fiber bundles, also known as imaging bundles, comprise typically tens of thousands of waveguiding glass or plastic cores surrounded by lower index material. Ideally, each fiber is considered to act as an independent waveguide, the whole array being contained within a diameter up to a few millimeters. Because fiber positions match at both ends of the bundle, an image projected onto the input face is transmitted unaltered to the output end. This is demonstrated by Fig. 2(a); an illuminated sheet of letter "e" stencils is imaged, with a magnification $M \approx 0.02$, onto the input face of an imaging bundle, and the output face is then imaged, with a magnification $M \approx 6$ onto a CCD camera. Imaging fiber bundles are manufactured both in silica and in crown glass [24]. There are several types: the illuminated end face of a wound bundle is shown, at a magnification of about $M \approx 40$, in Fig. 2(b). This type is made by winding subbundles of 5 × 5 fibers into a single-layer ribbon on a cylindrical mandrel, assembling layers in a separate laminating operation, then cutting through and polishing the ends [25]. These bundles typically have a diameter of 4–10 mm, and have been successfully used in flow measurement [26,27] and speckle [28] instrumentation applications in our laboratory. Fused bundles [Fig. 2(c)], in which the matrix of cores and cladding is solid along the entire length, are also available [29]. These typically have core diameters of a few micrometers, but are much

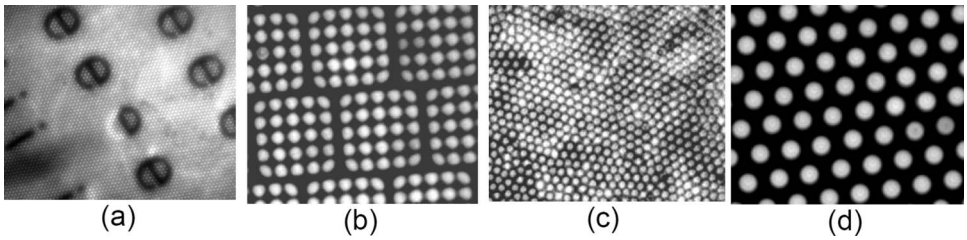

Fig. 2. CCD camera views of bundle end faces, under white-light transmission. (a) Image of a sheet of stencils (one "e" partially rubbed away), transmitted through a leached bundle. The magnification in this image is a factor of ~5 lower than in the previous three, but the hexagonal pattern of individual fiber cores can still just be distinguished. (b) Wound bundle; pixel size within subbundle is 10 μm. (c) Fused bundle; core diameter approximately 3 μm. (d) Leached fiber bundle used in this study; pixel diameter 10.6 μm, core diameter approximately 8 μm.

less flexible components, with a minimum bend radius of several centimeters. Also, we were unable to locate either wound or fused bundles in which it was possible to confine near-infrared (NIR) light to a single core over the length of the bundle.

Leached bundles [Fig. 2(d)] are manufactured by laying up rigid, double-clad core rods in a close-packed array, such that any particular core occupies the same position in the matrix at both ends of the bundle [30]. The entire assembly is then fused and drawn to reduce the core diameters. Over the entire bundle, apart from lengths of about 1 cm at either end, the outer layer of cladding is removed from each core by acid leaching, separating the fibers and rendering the bundle extremely flexible, and the faces of the short, rigid end sections are polished to obtain an optically flat finish [31]. Figure 3(a) illustrates the structure.

Many of the commercially available leached bundles have core diameters of up to several tens of micrometers, and a high degree of multimoding is to be expected within the fibers. This is not a problem for direct visualization of a white-light image by the eye, but does make such bundles unsuitable for use with laser sources and interferometric systems. Hence leached bundles, with much smaller core diameters of 6–12 μm (Schott North America), were selected for this investigation. The actual bundles used had a core center spacing, or pixel size, of 10.6 μm, as shown in Fig. 3(b).

Incorporating an imaging bundle into an OCT system creates challenges additional to those found in single-fiber OCT. The numerical aperture (NA) of bundles is generally at least 0.5 in the visible region of the spectrum, much greater than the value of 0.1–0.15 typical for single-mode fibers. This results from the need to confine the light adequately to an individual core surrounded by only a very thin layer of cladding, so that cross coupling between fibers is minimized. For typical core diameters, the result is multimode guiding behavior at wavelengths in the visible region of the spectrum. Wavelengths used for OCT are typically in the range of 400–1500 nm, with most being between 800 and 1300 nm. The bundle NA and number of modes supported in the NIR will be lower than in the visible but, as described below, a degree of multimode behavior persists up to at least 1400 nm. A high NA creates a number of issues. First, light must be delivered to and from the fiber bundle, and to the detector, using single-mode fiber components, such as couplers. The NA of these is poorly matched to the bundle NA, which inevitably leads to optical losses unless coupling to the bundle can be very carefully controlled, to excite only the fundamental mode of each core. Similarly, at the sample end of the OCT probe, it is desirable for the beam to have a rather small value of NA, to ensure sufficient depth of focus; too small a Rayleigh range results in excessive loss of contrast and lateral resolution away from the best-focus position in the OCT image. If more than one bundle mode is excited, NA matching here will again be poor.

Multimoding occurs then, even when bundles designed for the visible spectrum are used at wavelengths in the NIR. It is clearly very undesirable in an OCT system. Modes excited in addition to the fundamental will travel different path lengths within the bundle core, giving rise to unwanted signals in the OCT image. Provided that the difference in optical path length for two modes is within the instantaneous coherence length of the laser (about 10–20 mm for the Santec laser used here), then wavelength-dependent interference will occur between those modes, causing the output to oscillate. The frequency of oscillation will depend upon the fiber length and dispersion characteristics.

The modes excited in any particular core are affected by the coupling conditions [32]. The center wavelength of the swept source is considerably higher than the visible wavelengths for which the bundle is designed, which immediately reduces the number of supported modes. In addition, a low NA coupling lens, an incident beam well aligned normal to the bundle input face, and centering of the beam focus

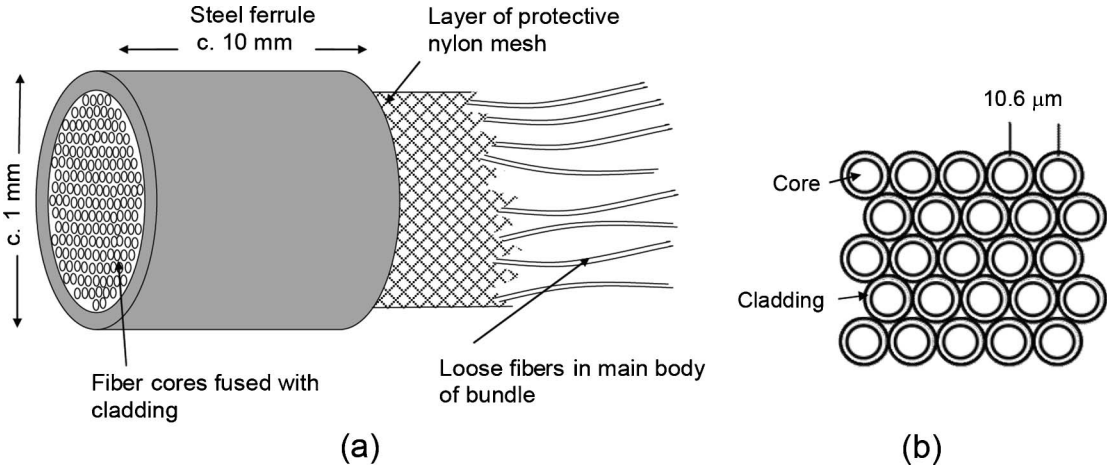

Fig. 3. (a) Construction of a leached fiber bundle, (b) hexagonal close-packed arrangement of fiber cores in the rigid end ferrules.

within the selected core, will result in near-single-mode behavior. However, it is not possible to ensure that these conditions apply at all times when scanning the input beam across the bundle face to access many bundle cores rapidly and sequentially.

Because the cladding thickness is very small compared with conventional fibers, some overlap of modal fields between cores is to be expected, particularly in the rigid end ferrules of the bundle [Fig. 3], where the fibers are hexagonally close packed and cores lie parallel in a matrix of cladding material over distances of several millimeters. As a result, a fraction of optical power will be coupled from the illuminated core into several neighboring cores. The degree of power transfer depends on the quality of phase matching between the two waveguides involved in the process; for identical fibers, power transfer could, in principle, be total over a sufficient interaction length, giving rise to severe cross-talk problems in the signal. In fused bundles, modeling has shown [33] that diameter variations occurring over distance within the bundle are helpful in providing a limitation on interaction length, and keeping the light largely confined to the core illuminated at the bundle input. In leached bundles of the type used for these experiments, diameter variations are very small, but the fibers lie in a loose skein outside the end ferrules of the bundle, which also places a limitation on coupling interaction length. However, because the cladding is only about 2 μm thick, it is possible that significant overlap of modal fields occurs even within the region of the bundle where the fibers are physically separated from one another by etching, in which case additional cross-coupling effects will occur.

A fill-factor loss of around 40% is generally quoted for imaging bundles. When the entire bundle face is illuminated at one time, as in typical visual inspection applications, light that falls in the regions between fiber cores is lost. It should be noted that this loss operates differently in the proposed OCT application. For ideal input coupling, the entire available power from the beam addresses individual bundle fibers, but there is a total loss of data when the beam addresses regions within the cladding. This

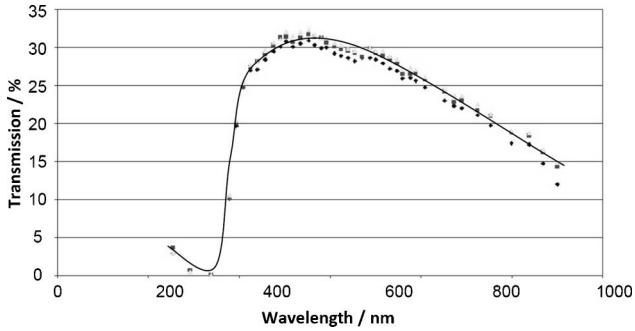

Fig. 4. Transmission characteristic of Schott leached bundle (plot provided by Schott North America) up to 1200 nm, for three sets of measurement, represented by square-, diamond-, and triangle-shaped markers, in 760 mm long bundles with 8.4 μm pixels. The superimposed curve is a visual fit added by the authors for greater clarity.

results in discretization of the image data. In these experiments, a powermeter has been used to measure the transmission loss experienced when coupling to a single bundle core. The value obtained is, of course, dependent on the quality of input coupling. For an input NA of about 0.15, a maximum transmission of about 17% was obtained in a 1.35 m long bundle at 1330 nm.

Transmission information is provided by the manufacturer [34] for wavelengths up to 1100 nm, as shown in Fig. 4. Maximum transmission occurs at about 500 nm, with the value gradually declining as wavelength increases. Our measured value looks reasonable when compared with this curve. In a double-pass arrangement, this equates to 97% loss of optical power in the bundle, which is a difficulty with this approach at the present time. Shorter bundles are available: we also measured the transmission for a 0.52 m long bundle at the same input NA. The measurement was not directly comparable, as the pixel size for this bundle was only 8.4 μm, compared with 10.6 μm for the longer bundle. However, an increased transmission of 27% was observed. The double-pass loss for this bundle is therefore 93%. It seems likely that the dominant loss mechanism is leakage from the cladding over the length of the

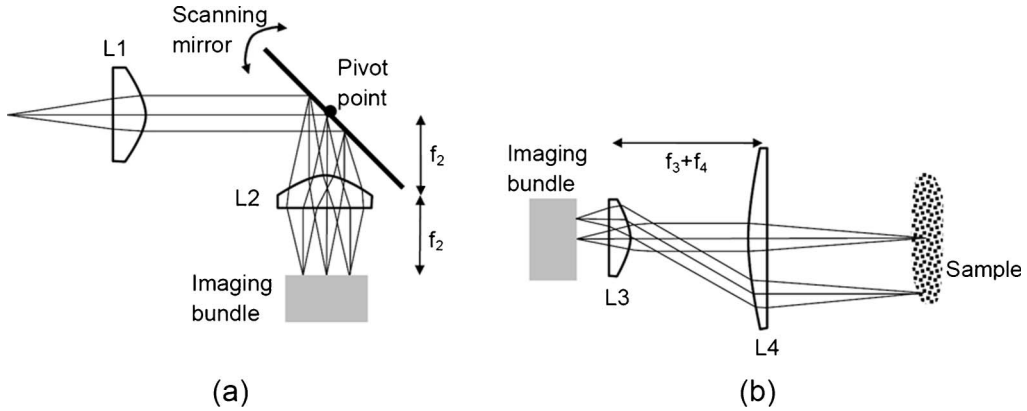

Fig. 5. (a) Lens arrangement for scanning onto input face of bundle, showing scanning mirror in front focal plane of focusing lens. (b) Telecentric lens arrangement in probe section of optical system; L, lens; f, focal length.

bundle, as a consequence of this layer being very thin in comparison with the cladding of a standard single-mode fiber.

4. Bundles in an OCT System

A. Lens Arrangements for Input and Output Coupling

The optimum input coupling arrangement for the bundle is to place the scanning mirror in the front focal plane of the coupling lens [Fig. 5(a)]. The chief ray within the focused beam then remains perpendicular to the bundle end face at all scan positions. This also ensures that the position of best focus is the same for all fibers in the bundle. For the scanning mirror at longer distances from this lens, poor beam focus and increased excitation of higher-order modes are experienced by fiber cores toward the extremes of the scan. Short focal length, aspheric lenses (Thorlabs, Inc.) were used in our system to keep the arrangement compact, and the design enabled all components to be mounted within a small bench footprint.

At the distal end of the bundle, similar considerations apply to the selection of lenses. A telecentric imaging system [Fig. 5(b)] is desirable, particularly where the reference beam is derived from this end of the probe, to ensure that the chief ray in the sample beam is parallel to the optical axis of the system for all image positions. This is not difficult to arrange on the laboratory bench, but requires lens L4 to have a clear aperture of 3–6 mm in diameter when used at a magnification of 2–3, and is therefore not so suitable when the system is designed for endoscopic applications in confined spaces. The depth of focus within the sample depends on beam NA; an acceptable Rayleigh range would be about 100–200 μm, which requires the NA to be about 0.07–0.05 at a wavelength of 1330 nm. This would provide reasonable imaging quality to a sample depth of more than 1 mm. If suppression of higher-order modes is achieved at the input, the output NA of the beam will be less than the standard value quoted for the bundle, but insufficiently low for good OCT imaging. Using an NIR CCD camera (Vosskhühler NIR-300 InGaAs sensor, 320 × 256 array of 30 μm square pixels), the output NA of light transmitted by a single core of the bundle was measured for input NA values ranging from about 0.15–0.55, close to the center of the mirror scan. In all cases, the NA of the output light was similar, with values ranging between about 0.12 and 0.15. This suggests that only a few modes are excited at these wavelengths, with most of the light propagating in the fundamental mode.

The modal patterns are most clearly observed under monochromatic illumination, thus, a fiber Bragg grating fabricated in our laboratories (wavelength 1301 nm, 40% reflectivity) was used to select a 0.2 nm wide slice from the swept-source output. This light was coupled, with an input NA of about 0.5, into a single-fiber core, and the modal pattern at the bundle output was observed by imaging the core of interest onto the CCD camera. Representative results are presented in Figs. 6(a)–6(d), along with profiles taken horizontally through the center of each image, for four slightly different coupling conditions [Figs. 6(e)–6(h)]. The gain is not the same for all these images; maximum optical power is transmitted in the situation depicted in Fig. 6(a).

When the beam is optimally focused and the beam waist concentrically aligned with the fiber [Figs. 6(a) and 6(e)], the output appears very similar to that of a single-mode fiber, with coupled power at a maximum and the profile of the mode almost Gaussian in form. However, a few micrometers of defocus or lateral offset causes some of the power to couple into higher-order modes. Only a few modes appear to be excited

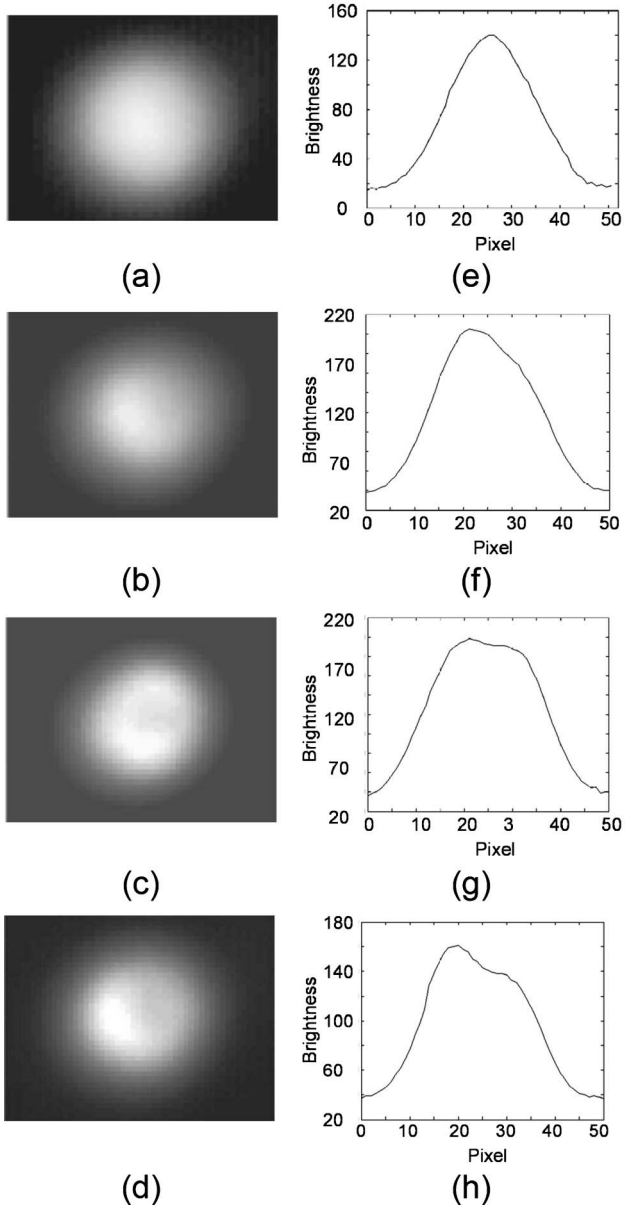

Fig. 6. (a)–(d) Near-field modal patterns ($M \approx 100$) and (e)–(h) horizontal profiles through the center of each image, showing the effect of input coupling conditions on modal population for a single core of fiber bundle.

to any appreciable extent under the coupling conditions experienced as the beam scans across the bundle, but even this small fraction of power traveling in other modes will cause artifacts and loss of signal-to-noise ratio (SNR) in the OCT images.

Some additional power loss is to be expected in the probe-end optics, in reducing the NA to a value appropriate for sample imaging. In single-fiber OCT systems, the region addressed on the sample surface is independent of the probe lenses, being determined by the angular excursions of one or two galvanometer mirrors. In bundle-based OCT, however, the area sampled is determined by the input and output NA values of the lens system used to image the distal bundle face onto the sample, and this is coupled to the magnification of the lens system. For a bundle diameter of 1 mm, a magnification M of about 2 would provide a reasonable sample dimension and an acceptable NA for the probe beam. It must be remembered that the number of sampling points (fiber cores) is fixed, so an increase in scan diameter on the sample implies an accompanying decrease in the lateral resolution. For the highest resolution, the sample dimension imaged must be equal to or less than the bundle diameter. For larger images, a bundle containing a larger number of fiber cores should be used. As magnification decreases, and lateral resolution increases, it becomes necessary to include an aperture stop to maintain depth of focus; however, a loss of optical power will be experienced, proportional to the square of the NA reduction ratio in the focused sample beam, and it may sometimes be preferable simply to accept a smaller imaging depth for high resolution images.

GRIN-rod lenses are an attractive alternative to conventional lenses, as their small size and cylindrical form allow for ease of mounting and compact, robust systems. GRIN-rod lenses generally have small amounts of spherical aberration and astigmatism, and some field curvature [35,36]. Chromatic aberration can be large, especially in the visible range, with focal shifts of up to 15–20 μm over about 100 nm, which imposes a limitation on depth resolution in ultrahigh resolution OCT systems, but this aberration is much lower in the NIR and performance is perfectly adequate for low-coherence imaging in the type of system described here.

B. Configuration 1: Bulk-Optic Michelson Interferometer at Distal End of Bundle

Several configurations for bundle-based systems have been investigated. Initially, the common-path system of Fig. 1 was used, in which a Michelson interferometer was formed using a 5 mm beam splitter cube positioned at the distal end of the bundle. This arrangement ensures polarization matching between the signal and reference beams, maximizing signal amplitude, and also ensures that both beams follow identical paths through the bundle. As discussed below, the resulting dispersion matching is a significant advantage of the common-path scheme. The lateral scanning of the reference beam that occurs in this system is less advantageous. When a flat reference mirror is used, power is lost toward the extremes of the scan due to increasing beam angle. The variation in power transmitted through individual fibers is also very variable, depending on coupling conditions at the bundle input. These effects make it difficult, even partially, to remove the DC component of the OCT signal, thereby limiting attainable SNR. Backreflections from both ends of the fiber bundle contribute significant DC levels to the detected signal, raising the excess noise.

Because losses are high for beams traveling within the bundle, the proximal face reflection was particularly troublesome, so 12° angled polishes were applied at the input and output faces of the bundle. Snell's law at the glass/air interface requires that the fiber interface then be tilted away from the optical axis. Setting the tilt angle of the bundle ends for maximum coupling into the angle-polished cores required care. There was also a loss of focus associated with the angled polish, toward extremes of the beam transit, both at the input and output of the bundle. At the input end, this can be minimized by the use of low NA optics. In principle, it could be eliminated by translating the bundle end parallel to the polished surface instead of beam scanning but, in practice, translation stages with hundreds of micrometers range, >100 Hz resonant frequencies and trajectory precision of a few micrometers are very costly. Unfortunately, suppression of the backreflection from the distal end was less successful, because of the multimode nature of the cores. There was a tendency for the angled polish to couple backreflected light into higher-order modes, which adversely affected the images by increasing modal interference artifacts.

Polishing the ends of the bundle normal to the optical axis, and having a V-type antireflection (AR) coating [37] applied (Vortex Optical Coatings Ltd.), was found to be a helpful alternative to angle-polishing, reducing the reflectivity of the fiber ends to about 0.004, from a value of about 0.05 for the uncoated surfaces. A more sophisticated coating would further reduce this value, although an angled polish still offers superior suppression at the beam input.

C. Configuration 2: Michelson Interferometer Formed between Two Bundles

To avoid the reference beam scanning inevitable in the common-path arrangement, the Michelson interferometer arrangement shown in Fig. 7(a) was also investigated. Initially, the reference arm comprised a single-mode fiber of similar length to the imaging bundle, with path-length trimming achieved in the short air paths at the distal ends of each arm. It was immediately clear from this setup that the effective index and dispersion of the single-mode fiber are very different from that of the bundle cores; the width of the OCT signal became dependent on the depth position within the image, and was significantly broadened for all depth positions. A

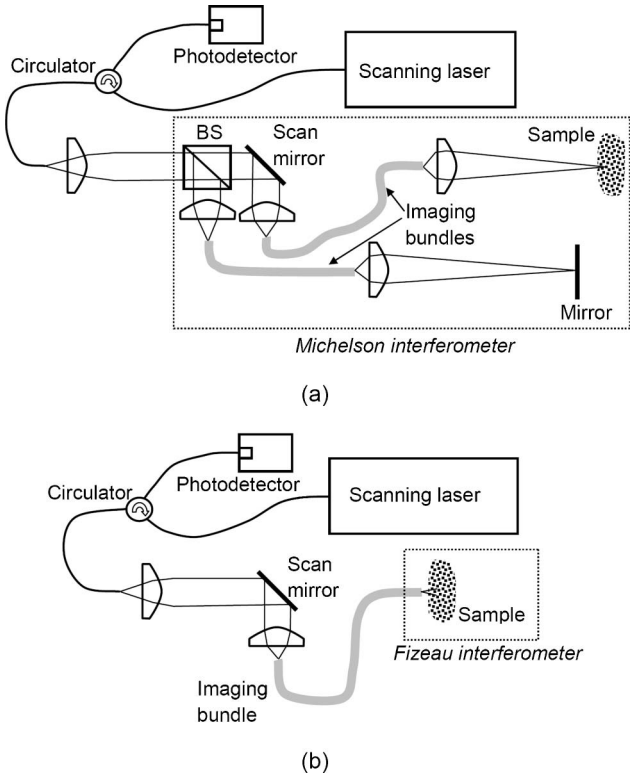

Fig. 7. Optical interferometer configurations used for low-coherence imaging; BM, beam splitter. (a) Configuration 2, Michelson interferometer using two separate bundles for reference and sample beams. (b) Configuration 3, Fizeau interferometer formed between output end of bundle and sample.

satisfactory image could not be obtained. The single-mode reference fiber was therefore replaced by a second imaging bundle of a type and length matching the first. Using a single fiber within this bundle as the guide for the reference beam resulted in a great improvement in image quality. Of course, it is an expensive solution to place a second bundle in the reference arm for the use of one fiber core. In principle, the same result could be achieved by coupling the reference beam into a peripheral fiber core of the main sample-arm bundle. This would be less straightforward to arrange experimentally, but not prohibitively difficult.

D. Configuration 3: Fizeau Interferometer at Distal End of Bundle

Finally, a third arrangement was investigated [Fig. 7(b)], which is attractive because it requires no additional optical components within the probe. The reference beam is derived from the internal reflection at the distal end of each fiber core. The beam from the output of the bundle is allowed simply to diverge until it strikes the sample. This technique has been reported in single-fiber systems [19,38]. Although the optical power does not converge to a beam waist, if the sample is positioned close enough to the end of the bundle, the beam will still be small enough for adequate imaging. The reference beam is derived from the distal bundle face, which, for an uncoated bundle, has a reflectivity of about 5%. If required, a higher percentage of light can be transferred into the reference beam by appropriate coating of the bundle face. This OCT configuration requires the object to be positioned very close to the end of the probe, as the maximum operating distance, limited by beam defocus, is a few hundred micrometers.

Balanced detection is often used in OCT to remove excess noise. Typical optical arrangements for single-fiber OCT systems are similar to Configuration 2 (Subsection 4.C). In such systems, balanced detection is achieved by collecting both outputs from the Michelson interferometer. The DC background common to both signals is largely removed, along with the excess noise, and the interferometric, antiphase signals combine additively. Although, in principle, the same technique can be applied in bundle-based systems, it is complicated by the multimode behavior of the bundle fiber cores. Unless all light from the returned signal in each multimode bundle core couples to the collection fiber of the detector, which is not generally the case, balanced detection will not be completely successful, as the coupling at this point will be wavelength dependent. Multimode collection fibers can be used with the balanced detector, but the photodetector dimension is only 0.1 mm, and similar problems occur if not all the power from the multimode fiber is transferred to the active detector area.

Partial removal of the DC signal component can be achieved in our system by splitting off a small portion of the output from the swept source using a 95/5 directional coupler, collecting the light on the second input of the balanced detector, and attenuating this beam until its magnitude closely matches that of the DC level in the OCT signal beam. In practice, however, little improvement in image quality is observed, because the detection limits of the system are dominated at present by image artifacts resulting from

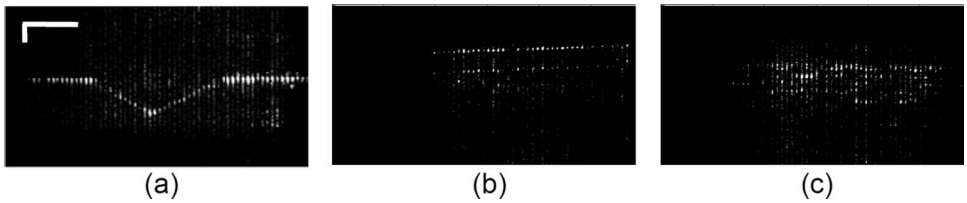

Fig. 8. Images from system Configuration 1. The samples represented are (a) a 680 μm-wide V-groove in a milled alloy block, (b) a sheet of translucent stencil film, and (c) the first few layers in a reel of adhesive tape. About 60 fibers are used. White bars show 250 μm, width and depth scales.

multimode behavior of the bundle cores. If multimoding were eliminated, detector or excess noise would become dominant, and DC reduction would then be more helpful. Reduction of excess noise is also affected by the interferometer arrangement used, and also depends on the extent to which the front-face reflection from the bundle can be suppressed.

5. Results and Discussion

Images were acquired for the three imaging system configurations described in Section 4, and are shown in Figs. 8–10. The magnification for Configurations 1 and 2 was arranged to be similar, to facilitate visual comparison of images of the same sample taken with different systems. In Configuration 3, unit magnification is intrinsic to the arrangement, since no additional optics are employed in the probe section of the instrument.

A. Configuration 1: Bulk-Optic Michelson Interferometer at Distal End of Bundle

The images shown in Fig. 8 exhibit a feature characteristic to all bundle-based low-coherence systems. Because of the "dead space" in the nonguiding cladding region between fibers, images have a vertically striped appearance, with bright lines corresponding to illuminated bundle fiber cores.

The magnification in this system was 2.4. The low-coherence interferometer was formed by including a beam splitter cube in the probe section of the system, to create two beam paths. The reference beam is backreflected from a mirror, and the sample is positioned at the focus of the other beam. By placing the beam splitter after the focusing optics, the number of lenses required is minimized, and the beam paths to the focal planes are automatically matched in the two arms. It should be noted that the cube has the effect of shifting the focal plane back by a distance of about 3.5 mm, as compared with the same system without a beam splitter; this must be accounted for during system setup. In our system, a beam splitter with a 70/20 power split ratio was used (approximately 10% loss), such that the straight-through (reference) beam contained about 20% of the incident power, and the reflected (sample) beam about 70%. After the double pass through this component experienced by both beams, the ratio of power returning from the sample and reference arms would be about 12:1 for equal reflectivity in each arm. Because, in practice, the reflectivity in the sample arm is typically much lower than that in the reference arm, the unequal split ratio helps to maximize efficient use of the available light. The Michelson configuration allows the sample to be positioned to either side of the zero path-length difference position. In all the images of Fig. 8, parts of the sample closest to the bundle appear toward the top of the image.

The prime advantage of Configuration 1 is the common-path arrangement. Reference and signal beams travel the same route through the bundle. Although this does not eliminate modal problems, it does minimize dispersion broadening of the interference signal, and polarization matching is automatically achieved at all times in all fibers. The main disadvantage is that the reference beam undergoes spatial scanning, which results in large intensity variation in this beam, in addition to those in the sample beam. Unless the telecentric probe lens arrangement of Fig. 5(b) is adopted, there will also be "walk-off" of the beam incident on the reference mirror toward the extremes of the scan. The effects of this can be seen in the images shown in Figs. 8(a)–8(c). The central portion of the image is bright, but loss of power toward the ends of the transverse scan means that this region of the image may be lost. The problem is least apparent in Fig. 8(a), where the sample is of very high reflectivity.

B. Configuration 2: Michelson Interferometer Formed between Two Bundles

The images acquired using this system, shown in Fig. 9, were of better quality in several ways than those acquired using the system previously described. The telecentric probe lens system of Fig. 5(b) was implemented, using lenses of $f = 8$ and 18.4 mm and it is clear, particularly from Fig. 9(a), that fading toward the edge of the image has been almost eliminated. It would similarly be possible to employ this lens system in Configuration 1, with the beam splitter positioned after the second lens. The contrast is also better in the images shown in Fig. 9, because physical separation of the reference and signal arms allowed optimized input coupling for the reference beam bundle to be achieved and maintained through a single-fiber core, while only the signal beam was scanned from one fiber to another. The magnification of the system was 2.3. In Fig. 9(f), an image acquired with the same source and electronics, but using single-mode fibers with probe-end scanning, is shown for comparison. The image demonstrates that, with advances in appropriate bundle

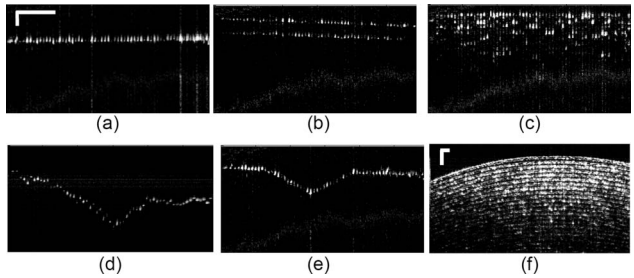

Fig. 9. Images from system Configuration 2. The samples represented are (a) a matte, milled metallic surface, (b) a sheet of translucent stencil film, (c) the first few layers in a reel of adhesive tape, and (d), (e) a 680 μm-wide V-groove in a milled alloy block. A correction has been applied to displayed depth positions in all images except for (d). About 60 fibers are used. White bars show 250 μm, width and depth scales. For comparison, a second image of the adhesive tape reel, acquired using our OCT system with a single fiber and a scanning mirror instead of the bundle, is shown in (f). The depth scale for this image is as for the others, but the lateral distance is greater at 6.5 mm.

transmission and modal characteristics, excellent image quality is achievable in such a system.

There is one drawback of this configuration. The individual optical paths for fibers within the bundle vary by a few tens of micrometers, even when the end faces are polished flat and perpendicular to the bundle axis. This introduces a distortion of the acquired image. Figure 9(d) shows an uncorrected image of a 680 μm-wide V groove. However, it is reasonably straightforward to correct for this distortion. A reference image taken from a flat surface is acquired. The depth positions of the maxima are computed, stored, and subtracted from the corresponding depth values in each subsequent set of acquisitions. The images shown in Figs. 9(a)–9(c) and 9(e) have all been adjusted using this correction. The reference data set is, of course, unique to the particular row of fiber cores used to acquire the 2D image, and must be renewed if a different row of fibers is selected.

C. Configuration 3: Fizeau Interferometer at Distal End of Bundle

This is the most straightforward system in terms of optical components and alignment. The light from the source is coupled directly into the bundle, via the transverse scanning mirror. At the probe end of the bundle, no additional optics are required and the magnification is therefore always 1.

The light exiting from the bundle is simply allowed to diverge until it strikes the sample, which is placed within a few hundred micrometers of the bundle tip. Focusing optics could be used at the end of the bundle, but the instantaneous coherence length of the Santec source is not large enough to permit this in our system. When a flat, matte-surface metallic sample is used as the sample, it appears that good imaging is achieved, as seen in Fig. 10(a). However, this is rather surprising, since the beam divergence is significant and, at a distance of 500 μm from the bundle, the beam diameter will be about 150 μm. This would be expected to cause severe power losses and reduction in transverse resolution. Indeed, when a more complex object is introduced, such as a 280 μm wide, machined V-groove [Fig. 10(b)], it becomes clear that good imaging is to be expected only for structures that are almost parallel to the end face of the bundle. Within the groove, where the path length changes appreciably over small lateral distances, the image becomes smeared out. It is possible to see that a hollow exists in the sample structure, but the exact form of the structure is lost.

This experiment was performed using a bundle with coated input and output faces. The reference reflectivity was about 0.4%. It would be straightforward to achieve a reference reflectivity of 4%–5%, using an uncoated glass interface, or a greater value by application of a high-reflectivity coating. Such a system could be used for thickness measurements, if the structures to be imaged are almost parallel to the bundle end face. A reasonable depth image was obtained, showing the first four layers within a reel of adhesive tape [Fig. 10(c)]. As in Configuration 1, polarization matching of signal and reference beams is automatic.

6. Discussion of System Performance

In OCT, sample-arm reflectivity values are typically around 10^{-5}–10^{-7}, therefore, excellent signal-to-noise performance is critical to achieving satisfactory image contrast throughout the image depth. Optimum performance depends on reducing detector and excess noise contributions to the point where the remaining shot noise is dominant. Detector noise is dependent on gain and bandwidth, and will typically be fixed for a given acquisition system, so detector SNR is maximized by selection of a low-noise detector in the first place, and then by maximizing the interferometric OCT signal. There is generally no lack of reference beam power but, for turbid sample materials, it is vital to maximize the much weaker coherent signal from the sample arm. It is important for imaging that reference beam power should be significantly greater than sample beam power; otherwise, the image will be confused by signals resulting from interference between various sample-arm reflections. The absolute magnitude of the interferometric signal can be boosted by further increasing reference beam power, in a manner analogous to that used in reference beam laser anemometry [39]. However, excess noise is proportional to the square of the mean DC signal component. This means that, if excess and detector noise are similar in magnitude, the increase in excess noise rapidly outweighs any improvement in detector SNR due to the increased reference beam component. Where balanced detection is used, much of the excess noise can be cancelled in Michelson-type arrangements, but a beat noise component remains.

Expressions for the various noise components are found in many publications. We refer to one example

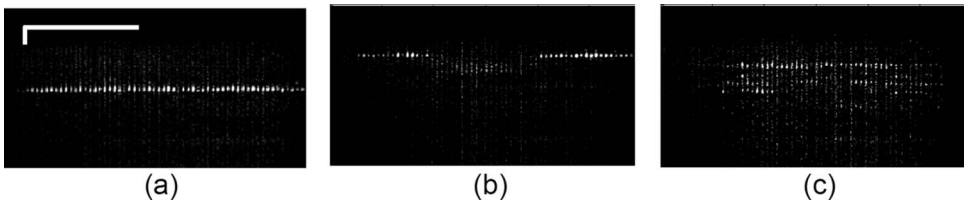

Fig. 10. Images from system shown in Configuration 3. The samples represented are (a) a matte, milled metallic surface, (b) a 280 μm-wide V-groove in a milled alloy block, and (c) the first few layers in a reel of adhesive tape. About 60 fibers are used. White bars show 250 μm, width and depth scales.

[40], with the magnitudes of the noise components adjusted for our different interferometer configurations. For the detector used in this project, the noise over the 3 dB bandwidth, expressed as the variance of the current, is about 2.0×10^{-16} A^2. For Configurations 1 and 2, with optimal alignment, and using the 70/20 beam splitter, a typical optical power of 10 μW is obtained at the detector from the reference arm of the interferometer. If we assume that the maximum SNR is obtained when the signal power at the detector equals the reference power, we can calculate a mean square OCT signal magnitude of about 10^{-10} A^2, a shot-noise variance of 4.8×10^{-17} A^2 and, ignoring polarization effects, an excess noise variance of about 10^{-16} A^2. These values are sometimes elevated by a relatively large residual front-face reflection from the bundle.

However, imaging is also affected by artifacts resulting from other effects. First, the raw laser wavelength profile is roughly sawtooth-shaped, although this is modified in the OCT system by wavelength-dependent coupling and fiber losses. It also carries some high-frequency structure, as shown in Fig. 11(a), which is more significant toward the high-wavelength end of the sweep. These features lead to unwanted lines in the Fourier transform image in Fig. 11(d). Because the bundle loss is high, great care must be taken to avoid even much-attenuated backreflections from elements such as neutral density filters placed between the laser and the bundle. The front-face reflection from the bundle is a particular problem, as discussed above.

A larger contribution to image artifacts comes from oscillatory effects due to multimoding and cross coupling in the bundle. Where these fall within the range of expected OCT frequencies, a spurious structure will appear at the corresponding depth in the FFT image, and the magnitude of these artifacts can be much larger than any of the noise sources in the system. Unwanted oscillations are present in the output when light is coupled into a single-fiber core, resulting in artifacts throughout the entire range of the Fourier transform image. The magnitude of the different frequencies present varies as the input coupling conditions are adjusted. Figure 11 shows the effect on the profile with coupling adjusted for (b), (e) minimal and (c), (f) more severe occurrence of artifacts. For Configurations 1 and 2, with the reference power at the detector as quoted above, these effects correspond to a variance of about 3×10^{-13} A^2. Bundle-induced effects therefore limit the actual SNR to about 25 dB, which is in agreement with observed values. Without such effects, the equivalent SNR would be closer to 60 dB. In the Fizeau configuration, all light from the circulator is coupled directly into the bundle via the scanning mirror; therefore, the reference beam, derived from reflection at the coated distal face of the bundle, is now weaker relative to the unwanted front-face reflection. This increases excess noise, but bundle-induced effects are still dominant overall, and are once again the limiting factor in the system. Hence the observed SNR is similar in all three configurations.

An approximate modal analysis was performed, using the linearly polarized mode approximation, to estimate the propagation constants for the two lowest-order modes of the bundle cores at the 1330 nm center wavelength. Exact figures for the refractive index of core and cladding were not known, but the measured output NA, and the fact that most optical power appears to be contained within a few low-order modes, are consistent with a V value of about 4. With these assumptions, the group delay difference between the two lowest-order modes

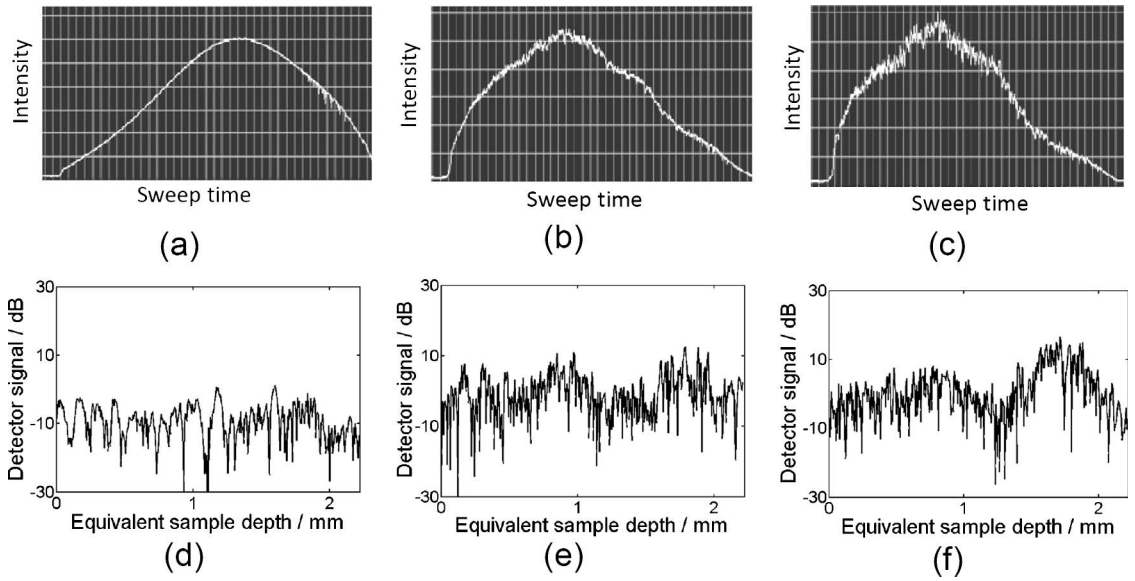

Fig. 11. Profile of detected signal after transmission of laser output through (a) a single-mode fiber, (b) a bundle core, with coupling adjusted to minimize artifacts, (c) a bundle core, with coupling adjusted to show more severe occurrence of artifacts. (d)–(f) Corresponding OCT signals, calculated from (a)–(c), respectively.

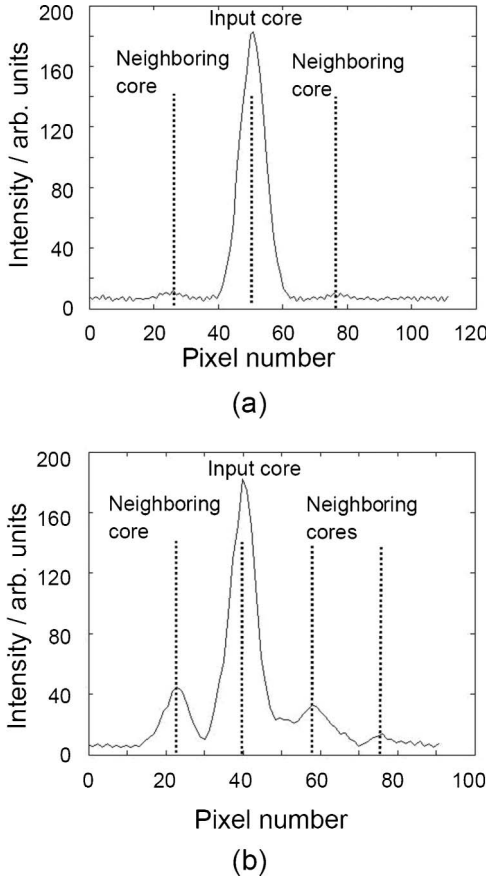

Fig. 12. Profile through modal pattern (core spacing 25 camera pixels at this magnification) from fiber core, for optimized input coupling, showing cross coupling of power to nearest-neighbor fibers at (a) 1330 nm and (b) 1550 nm.

suggests a path-length difference of about 8 mm for the 1350 mm long bundle. This is within the 10–20 mm coherence length of the swept source and confirms that interference effects between different modes are to be expected. Waveguide dispersion is relatively insignificant, but it is not possible to calculate exact oscillation frequencies because material dispersion, which is usually much larger than waveguide dispersion in fibers, is not known for the bundle. As the laser sweeps, the relative phase between the modes changes, causing the output intensity to oscillate. Oscillation in the 100 kHz–10 MHz range, depending on material dispersion, is predicted within the laser sweep range for interference between the two lowest-order modes. However, interference between a single pair of modes would be expected to produce only a single artifact at a fixed depth position in the image. In fact, the number of lines present implies that interference is taking place between multiple pairs of modes, or over multiple path-length differences. A large number of modes present would be necessary to explain the numerous unwanted frequencies present in the signal, so an additional mechanism is implied. Wavelength-dependent cross coupling between the primary fiber core and neighboring fibers is a possible explanation. There is indeed a small but significant degree of coupling between the primary core and the six adjacent fiber cores. When light was coupled into a single core within the bundle, a small amount of power was observed on the NIR CCD camera, emerging from neighboring cores. Figure 12(a) is a profile from a camera image, showing the output from the bundle when light is coupled into a single fiber so as to excite primarily the fundamental mode. In this situation, it can be seen that a small amount of power emerges from one or more of the neighboring cores, with a maximum of about 1.5% of the total output power appearing in any one of the six nearest neighbors.

Fiber-to-fiber cross coupling would be expected to be greater for higher-order modes, so interference effects caused by recoupling to the original fiber core should be reduced by choosing a collection lens NA close to the NA of the fundamental mode. However, there will be remaining wavelength-dependent variations, in both input coupling and cross coupling between fibers, which will also contribute to the spurious structures seen in images.

In practice, the oscillations caused by intermodal and cross-coupling effects dominate other noise sources in the system and, unfortunately, it is not possible to eliminate them other than by altering the design of the fiber bundle. The rms magnitude of the spurious oscillations is roughly equivalent to a sample reflection of about 0.01%, which is high enough to obscure interferometric signals from typical biological tissue samples. However, this does not prevent the technique from being useful in surface-profiling applications, or for semitransparent, nonbiological samples.

It might appear that an increase in the laser source wavelength (or reduction in core diameter) would improve performance, by eliminating the ability of the bundle fibers to support higher-order modes. However, the relatively small cladding layer between the cores causes cross coupling to increase as the wavelength approaches the single-mode cutoff; at a source wavelength of 1550 nm, a much larger fraction of light injected into a single-fiber core is cross coupled into surrounding fibers, and emerges at the distal end of the bundle from the six neighboring cores, as can be seen in Fig. 12(b). Improvement would, however, be achieved by a design of imaging bundle, with both smaller core diameter and a greater cladding thickness separating the cores [41]. Optical absorbers in the cladding region would reduce cross coupling still further. Although the “dead space” in the image would be greater from such a bundle, smoothing could be applied to improve image appearance [21], and lateral resolution could be adjusted via magnification of the probe optics. If intermodal effects could be eliminated, and an increase in the transmission of the bundles in the NIR portion of the spectrum achieved, a large performance improvement would result.

7. Conclusions

The perceived advantages of eliminating scanning components from the endoscope section of an OCT instrument have led to this investigation of systems using imaging fiber bundles. Leached fiber imaging bundles have been incorporated into swept-source OCT systems, using a variety of optical configurations, and images have been obtained from test objects with all three proposed configurations. The systems differ from single-fiber, scanned systems, in that images are affected by multimoding, cross coupling, and loss in the bundle cores. Removal of DC background, and elimination of unwanted reflections, is also more complex in bundle-based systems than in standard single-fiber configurations with probe-tip scanning. The relative merits of three possible optical configurations have been compared, and suggestions made for methods to suppress back-reflections from the bundle ends, by a combination of angle polishing and application of AR coatings. Characteristics of the leached bundles selected for this study have been investigated, and the way in which each affects image quality has been discussed. It is unlikely that the multimoding problem can be overcome completely without loss of spatial resolution in such systems, but changes in bundle design, to reduce losses and multimoding, would improve performance for low-coherence imaging applications.

This work has been supported by a grant (EP/F034679/1) from the UK Engineering and Physical Sciences Research Council (EPSRC).

References

1. B. L. Danielson and C. D. Whittenberg, "Guided-wave reflectometry with micrometer resolution," Appl. Opt. **26**, 2836–2842 (1987).
2. R. C. Youngquist, S. Carr, and D. E. N. Davies, "Optical coherence domain reflectometry: a new optical evaluation technique," Opt. Lett. **12**, 158–160 (1987).
3. I. Balboa, H. D. Ford, and R. P. Tatam, "Low-coherence optical fibre speckle interferometry," Meas. Sci. Technol. **17**, 605–616 (2006).
4. A. F. Fercher, C. Hitzenberger, and M. Juchen, "Measurement of intraocular optical distances using partially coherent laser light," J. Mod. Opt. **38**, 1327–1333 (1991).
5. J. G. Fujimoto, "Optical coherence tomography for ultrahigh resolution *in-vivo* imaging," Nat. Biotechnol. **21**, 1361–1367.
6. M. A. Choma, M. V. Sarunic, C. H. Yang, and J. A. Izatt, "Sensitivity advantage of swept source and Fourier domain optical coherence tomography," Opt. Express **11**, 2183–2189 (2003).
7. S.-W. Huang, A. D. Aguirre, R. A. Huber, D. C. Adler, and J. G. Fujimoto, "Swept source optical coherence tomography using a Fourier domain mode-locked laser," Opt. Express **15**, 6210–6217 (2007).
8. E. A. Swanson, J. A. Izatt, M. R. Hee, D. Huang, C. P. Lin, J. S. Schuman, and J. G. Fujimoto, "*In-vivo* retinal imaging by optical coherence tomography," Opt. Lett. **18**, 1864–1866 (1993).
9. A. F. Fercher, W. Drexler, C. K. Hitzenberger, and T. Lasser, "Optical coherence tomography—principles and applications," Rep. Prog. Phys. **66**, 239–303 (2003).
10. S. A. Boppart, W. Luo, D. L. Marks, and K. W. Singletary, "Optical coherence tomography: feasibility for basic research and image-guided surgery of breast cancer," Breast Cancer Res. Treat. **84**, 85–97 (2004).
11. P. H. Tran, D. S. Mukai, M. Brenner, and Z. Chen, "*In-vivo* endoscopic optical coherence tomography by use of a rotational microelectromechanical system probe," Opt. Lett. **29**, 1236–1238 (2004).
12. G. J. Tearney, S. A. Boppart, B. E. Bouma, M. E. Brezinski, N. J. Weissman, J. F. Southern, and J. G. Fujimoto, "Scanning single mode fiber optic catheter-endoscope for optical coherence tomography," Opt. Lett. **21**, 543–545 (1996).
13. Y. Zu, J. Singh, C. S. Premachandran, A. Khairyanto, K. W. S. Chen, N. Chen, C. J. R. Sheppard, and M. Olivo, "Design and development of a 3D scanning MEMS OCT probe using a novel SiOB package assembly," J. Micromech. Microeng. **18**, 125005 (2008).
14. D. Stifter, K. Wiesauer, M. Wurm, E. Schlotthauer, J. Kastner, M. Pircher, E. Gotzinger, and C. K. Hitzenberger, "Investigation of polymer and polymer/fibre composite materials with optical coherence tomography," Meas. Sci. Technol. **19**, 074011 (2008).
15. E. Alarousu, L. Krehut, T. Prykäri, and R. Myllylä, "Study on the use of optical coherence tomography in measurements of paper properties," Meas. Sci. Technol. **16**, 1131–1137 (2005).
16. H. Liang, M. Cid, R. Cucu, G. Dobre, A. Podoleanu, J. Pedro, and D. Saunders, "En-face optical coherence tomography—a novel application of non-invasive imaging to art conservation," Opt. Express **13**, 6133–6144 (2005).
17. H. D. Ford and R. P. Tatam, "Full-field optical coherence tomography," Proc. SPIE **5858**, 148–156 (2005).
18. T. Xie, D. Mukai, S. Guo, M. Brenner, and Z. Chen, "Fiber-optic-bundle-based optical coherence tomography," Opt. Lett. **30**, 1803–1805 (2005).
19. H. D. Ford and R. P. Tatam, "Fibre imaging bundles for full-field optical coherence tomography," Meas. Sci. Technol. **18**, 2949–2957 (2007).
20. J. U. Kang, J.-H. Han, X. Liu, and K. Zhang, "Common-path optical coherence tomography for biomedical imaging and sensing," J. Opt. Soc. Korea **14**, 1–13 (2010).
21. J.-H. Han, J. Lee, and J. U. Kang, "Pixelation effect removal from fiber bundle probe based optical coherence tomography imaging," Opt. Express **18**, 7427–7439 (2010).
22. P. Casaubieilh, H. D. Ford, and R. P. Tatam, "Optical fibre Fizeau-based OCT," Proc. SPIE **5502**, 338–41 (2004).
23. D. Heard, Santec Europe Ltd., Magdalen Centre, Robert Robinson Ave., Oxford Science Park, OX4 4GA (personal communication, 2008).
24. J. A. Udovich, N. D. Kirkpatrick, A. Kano, A. Tanbakuchi, U. Utzinger, and A. F. Gmitro, "Spectral background and transmission characteristics of fiber optic imaging bundles," Appl. Opt. **47**, 4560–4568 (2008).
25. "Wound image bundles," http://www.schott.com/lightingimaging/english/products/healthcare/imagingfiberoptics/flexiblecomponents/wound.html (Accessed October 2010).
26. D. S. Nobes, H. D. Ford, and R. P. Tatam, "Three component planar Doppler velocimetry using imaging fibre bundles," Exp. Fluids **36**, 3–10 (2004).
27. Z.-H. Lu, T. O. H. Charrett, and R. P. Tatam, "Three-component planar velocity measurements using Mach-Zehnder interferometric, filter-based planar Doppler velocimetry (MZI-PDV)," Meas. Sci. Technol. **20**, 034019 (2009).
28. D. Francis, S. W. James, and R. P. Tatam, "Surface strain measurement of rotating objects using pulsed laser shearography with coherent fibre-optic imaging bundles," Meas. Sci. Technol. **19**, 105301 (2008).
29. "Image Fiber," http://www.fujikura.com/prod/imagefiber/p1_1.html (Accessed January 2011).

30. "Transmitting images," http://www.schott.com/lightingimaging/english/life-science/medical-products/transmitting-images.html (Accessed October 2010).
31. K. Gerstner, A. Plichta, D. Schlatterbeck, M. Weisser, P. Brix, M. Sommer, R. Rubino, J. Bonja, R. Strack, I. Henze, and P. Arsenault, "Method of manufacturing a leached fiber bundle," U.S. patent 7,308,807 (18 December 2007).
32. S. K. Khijwania, F. D. Carter, J. T. Foley, and J. P. Singh, "Effect of launching condition on modal power characteristics of multi-mode step-index optical fiber: a theoretical and experimental investigation," Fiber Integr. Opt. **29**, 62–75 (2010).
33. K. L. Reichenbach and C. Xu, "Numerical analysis of light propagation in image fibers or coherent fiber bundles," Opt. Express **15**, 2151–2165 (2007).
34. K. Bhura, Schott North America, Inc., 122 Charlton Street, Southbridge, Mass. 01550 (personal communication, November 2008).
35. W. J. Tomlinson, "Aberrations of GRIN-rod lenses in multimode optical fiber devices," Appl. Opt. **19**, 1117–1126 (1980).
36. "GrinTech datasheets," http://www.grintech.de/downloads.html (Accessed October 2010).
37. "Coatings," www.photonicsolutions.co.uk/datasheets/casi/CXCoatings.pdf (Accessed October 2010).
38. U. Sharma and J. U. Kang, "Common-path OCT with side-viewing bare fiber probe for endoscopic OCT," Rev. Sci. Instrum. **78**, 113102 (2007).
39. D. Jackson and D. M. Paul, "Measurement of supersonic velocity and turbulence by laser anemometry," J. Phys. E **4**, 173–177 (1971).
40. X. Li, J.-H. Han, X. Liu, and J. H. Kang, "Signal-to-noise ratio analysis of all-fiber common-path optical coherence tomography," Appl. Opt. **47**, 4833–4840 (2008).
41. N. Ortega-Quijano, F. Fanjul-Vélez, and J. L. Arce-Diego, "Optical crosstalk influence in fiber imaging endoscopes design," Opt. Commun. **283**, 633–638 (2010).